Allan deviation tells the binding properties in single-molecule sensing with whispering-gallery-mode optical microcavities

Deshui Yu ● and Frank Vollmer

Living Systems Institute, Physics and Astronomy, University of Exeter, Exeter EX4 4QD, United Kingdom

We propose a scheme of exploring the kinetic properties of the receptor-ligand binding process by means of the frequency stability measurement of a whispering-gallery-mode optical microcavity. In this scheme, the probe beam is directly locked to the microcavity and the time resolution of the sensing detection is determined by the feedback loop response time $10\,\mu$s, which is much shorter than the current limit of about 20 ms. The receptor-ligand interactions are entirely mapped onto the probe light frequency and can be recovered through the analysis of its Allan deviation. As a result, one can investigate a chemical and biological reaction at the single-molecule level without the need for resolving the occurrence and duration of individual binding events. We numerically study this sensing scheme based on a practical optoplasmonic platform, where several gold nanorods are adsorbed onto the surface of a spherical microcavity that is located in the aqueous environment. The microsphere has a typical radius of $40\,\mu$m and quality factor of 10^6 (finesse of 2.6×10^3) at the wavelength of 785 nm. This powerful scheme may extend single-molecule sensing to the kinetic regime of the biochemical reactions.

I. INTRODUCTION

Owing to the properties of tight light confinement and high Q factor, whispering-gallery-mode (WGM) microcavities have been extensively used in chemical and biological sensing [1]. The fundamental sensing mechanism lies in the spectral shift $\delta\lambda$ and broadening of a WGM induced by the variation in the refractive index of the surrounding environment of a passive/active microcavity [2,3]. For a WGM at the wavelength $\lambda_{\rm cav}$, a dielectric nanoparticle with an excess polarizability $\alpha_{\rm ex}$ and a volume V_p leads to

$$\frac{\delta\lambda}{\lambda_{\rm cav}} = \frac{V_p}{V_{\rm cav}}\frac{\alpha_{\rm ex}}{2\varepsilon_0} \quad\text{with}\quad V_{\rm cav} = \frac{\int \epsilon(\mathbf{r})|\mathbf{E}(\mathbf{r})|^2 d\mathbf{r}}{|\mathbf{E}(\mathbf{r}_0)|^2}, \quad (1)$$

where ε_0 is the vacuum permittivity, $\epsilon(\mathbf{r})$ denotes the spatial distribution of the relative permittivity, and $\mathbf{E}(\mathbf{r})$ represents the WGM field. The mode volume $V_{\rm cav}$ of the WGM is evaluated based on the field intensity at the nanoparticle's position $\mathbf{r}_0$. Measuring $\delta\lambda$ allows one to estimate $\alpha_{\rm ex}$ or the nanoparticle's size. For example, a silica (refractive index of 1.45) microsphere has a typical radius $R_{\rm cav} = 40$ μm and is situated in the air. The mode volume of the fundamental TE-polarized WGM at $\lambda_{\rm cav} = 785$ nm is computed as $V_{\rm cav} = 2 \times 10^3$ μm^3. A spherical polystyrene nanoparticle with a radius of 50 nm and $\alpha_{\rm ex}/\varepsilon_0 = 1.2$ yields $\delta\lambda = 40$ fm,

i.e., $|\delta\lambda/\lambda_{\rm cav}| \sim 10^{-7}$. Besides dielectric nanoparticles, this mode-shift sensing mechanism is also applied to detect large single bioparticles, such as influenza viruses with $|\delta\lambda/\lambda_{\rm cav}| \sim 10^{-8}$ [4]. However, detecting small single biomolecules (e.g., proteins and short DNA) demands a further suppression of $V_{\rm cav}$.

Reducing $R_{\rm cav}$ can strengthen the evanescent field $\mathbf{E}(\mathbf{r}_0)$, thereby suppressing $V_{\rm cav}$ and enhancing $\delta\lambda$ [3,4]. However, the microcavity's Q factor also suffers from a large degradation due to increased radiation and surface scattering losses. An efficient measurement on $\delta\lambda$ requires the Q factor (linewidth $\kappa_0 = \omega_{\rm cav}/Q$ with $\omega_{\rm cav} = 2\pi c/\lambda_{\rm cav}$) of a microcavity to be sufficiently high (narrow). Generally, the Q factor of a WGM microcavity in the air reaches over 10^8 [5–7], corresponding to a finesse $F = 2.6 \times 10^5$ and linewidth $\kappa_0 = 2\pi \times 4$ MHz of a WGM at $\lambda_{\rm cav} = 785$ nm with $R_{\rm cav} = 40$ μm. However, detecting single biomolecules usually requires the microcavity to be immersed in an aqueous solution. This results in a serious degradation of the microcavity's Q factor, for instance, from 10^8 in the air to 10^6 in the water [8], because of the huge absorption losses in the aqueous environment. Reducing $R_{\rm cav}$ may further degrade Q, thereby deteriorating the sensor's performance.

The mode volume $V_{\rm cav}$ can, alternatively, be suppressed by hybridizing the localized surface plasmon resonance (LSPR), i.e., the collective oscillation of free electrons in nanostructured metals, with WGM microcavities [Fig. 1(a)]. The LSPR allows the subwavelength light confinement beyond the diffraction limit, boosting the local evanescent field $\mathbf{E}(\mathbf{r}_0)$. For example, a gold nanorod, whose circular cross-section diameter and length are 10 nm and 35 nm, respectively, gives a near-field intensity enhancement factor $\Lambda \sim 10^3$ around two hotspots [9]. Here, the plasmonic hotspots denote the regions
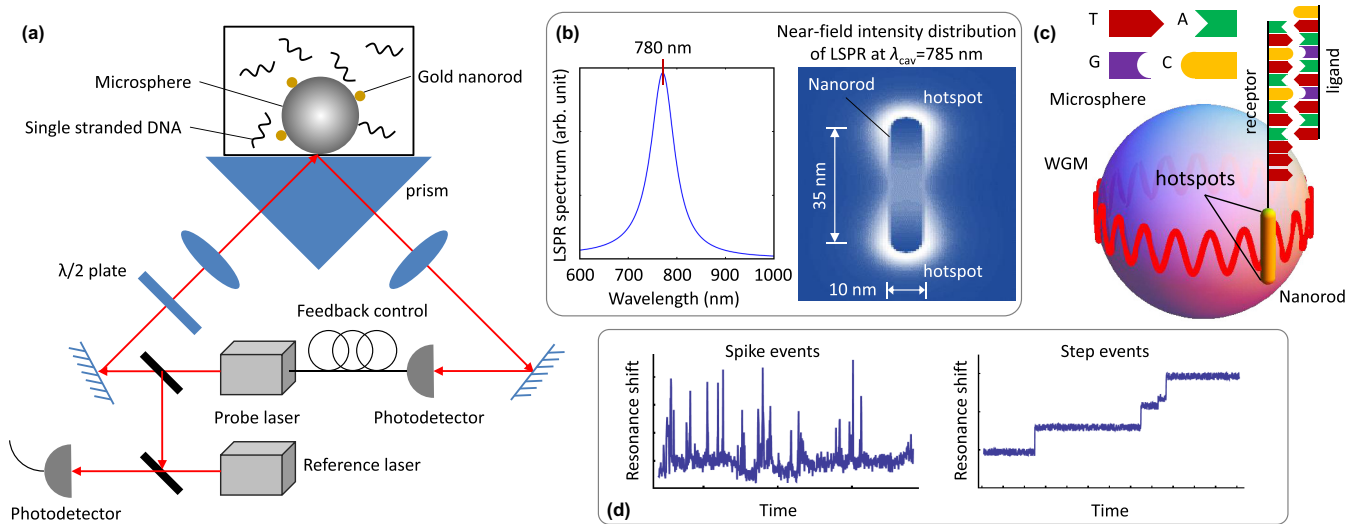
FIG. 1. (a) Single-molecule detection based on the optoplasmonic hybridization. A silica microsphere with a radius of $R_{cav} = 40\ \mu m$ is situated in the aqueous environment. Several gold nanorods are adsorbed onto the microsphere's surface. The TE-polarized cw and ccw WGMs at $\lambda_{cav} = 785$ nm are excited by a probe laser through an optical prism. The transmitted light is fed back into the probe laser, locking its frequency to the microcavity. The Allan deviation of the probe laser is measured by the beat note with a reference laser. (b) Longitudinal LSPR spectrum of a gold nanorod and the electric-field intensity distribution of LSPR at λ_{cav}. The circular cross section of the nanorod has a diameter of 10 nm and the nanorod's length is 35 nm. The regions around two ends of the nanorod are termed the hotspots, where the near-field intensity is strongly enhanced by a factor $\Lambda = 800$. (c) Evanescent interaction between the microsphere and a gold nanorod. The receptor molecules, which interact with the ligand molecules, are permanently attached within the nanorod's hotspots. (d) Schematic diagrams of the time traces of the wavelength shift of a WGM. The spike events correspond to the transient receptor-ligand interactions while the step events denote the permanent binding between single receptor and ligand molecules.

near sharp corners and tips of metal nanoparticles [Fig. 1(b)]. In addition, Ohmic losses of metal nanoparticles introduce an extra decay channel of intracavity photons, degrading the Q factor of microcavities. For instance, binding five gold nanorods, which are all aligned perpendicularly to the equatorial WGM, onto a microsphere immersed in the water may reduce Q from 1×10^6 to 5×10^5. Nevertheless, the large intensity enhancement factor Λ still strongly enhances the sensor's sensitivity.

Moreover, modifying the surface of metal nanoparticles with receptor (R) molecules enables a label-free detection of specific ligand (L) molecules [Fig. 1(c)] through the relevant binding reaction,

$$R + L \underset{k_{off}}{\overset{k_{on}}{\rightleftharpoons}} RL, \qquad (2)$$

much simplifying the sensing procedures. Here, k_{on} (in units of $M^{-1}s^{-1}$, where M denotes molar) and k_{off} (in units of s^{-1}) are the on-rate and off-rate constants, respectively. The single-molecule detection based on the optoplasmonic hybridization has been demonstrated for short DNA oligonucleotides [9], bovine serum albumin protein molecules [10], and even atomic ions, such as Zn^{2+} and Hg^{2+} [11], whose ionic radii are 0.74 and 1.02 Å, respectively. This is the highest sensitivity achieved by WGM microcavities so far. Recently, these optoplasmonic devices have been widely applied to monitor the reaction kinetics between receptor and ligand molecules in a label-free manner [12–14].

For conventional optoplasmonic sensors, the transmission spectrum of a WGM microcavity is measured by sweeping the wavelength of a probe laser. The single-molecule interactions are identified by the spike and step events [Fig. 1(d)] extracted, i.e., through fitting the spectrum to a Lorentzian profile, from a time trace of the WGM wavelength λ_{cav}. When a ligand molecule binds to a receptor molecule, λ_{cav} experiences a shift $\delta\lambda$ that is determined by Eq. (1). For a transient receptor-ligand interaction, $\delta\lambda$ vanishes once the ligand molecule is removed from the receptor molecule, leaving a spike in the time trace of λ_{cav}. By contrast, a step event occurs for a permanent receptor-ligand binding. The typical time resolution of the sensing detection is about tens of ms (e.g., 20 ms in [11–14]), which is limited by the scanning rate of the probe laser. To accurately capture the transmission spectrum of the microcavity, the probe laser frequency goes over the central frequency of the WGM with a width larger than κ_0. Also, the laser scanning should be slow enough that the intracavity field continuously maintains a steady state, i.e., adiabatic limit.

The adjacent single-molecule events with an interval shorter than the time resolution cannot be distinguished. Thus, the sensor's applications are restricted to an aqueous solution of ligand molecules with an appropriate off-rate constant k_{off} (e.g., $k_{off} = 47$ and $23\ s^{-1}$ in [13]) and also at a suitably low concentration (fM $\sim$ nM in [11–14]) with an appropriate on-rate constant k_{on}. This weakness may be overcome by directly locking the probe beam to the microcavity. The frequency locking time can be as short as $10\ \mu s$ [15], leading to a three-orders-of-magnitude improvement in the time resolution.

Moreover, extracting the spike and step events from a time trace of the WGM wavelength is usually implemented in a manual manner [11–14]. An empirical algorithm is applied to remove the background fluctuations and drift of the probe

laser [11]. However, it inevitably omits the weak spike/step events that are buried in the background noise and is thereby unable to reveal the entire picture of the chemical and biological reaction. To address this issue, the spike and step events may be treated as the extra noise to the microcavity and one performs the stability analysis on the probe beam whose frequency is locked to the microcavity.

In this paper, we numerically study a fast and sensitive single-molecule detection scheme. The probe beam is directly locked to the microcavity and the kinetic properties of the receptor-ligand binding interactions are explored by measuring the frequency stability, i.e., Allan deviation, of the probe light. This scheme is capable of capturing those single-molecule events with a duration of $10\,\mu$s, limited by the integration time of the feedback loop. The sensing method is applicable to the previously inaccessible kinetic regime with large on-rate k_{on} (at a high ligand concentration) and off-rate k_{off} constants.

II. PHYSICAL MODEL

The single-molecule sensing scheme is illustrated in Fig. 1(a). The light from a probe laser (amplitude $\mathcal{A}_p$ and frequency ω_p) is evanescently coupled into a silica microsphere via the total internal reflection at the surface of an optical prism. The microsphere-prism coupling rate is κ_{in}. The microsphere with a typical radius $R_{\text{cav}} = 40\,\mu$m is immersed in the water (refractive index of $n = 1.33$). The probe beam excites two degenerate fundamental clockwise (cw) and counterclockwise (ccw) WGMs (mode index $l = 453$) at $\lambda_{\text{cav}} = 785$ nm. Both WGMs are TE-polarized and their quality factor in the aqueous environment approximates $Q = 10^6$. The loss rate of two WGMs is $\kappa_0 = \omega_{\text{cav}}/Q$ with $\omega_{\text{cav}} = 2\pi c/\lambda_{\text{cav}}$. We assume a weak microsphere-prism coupling, i.e., $\kappa_{\text{in}} \ll \kappa_0$. The mode volume of the microcavity is computed as $V_{\text{cav}} = 7.2 \times 10^3\,\mu$m^3.

The light transmitted from the microsphere is measured by a photodetector. Unlike conventional optoplasmonic sensors [11–14], the output from the photodetector is further fed back into the probe laser system through a servo, locking the probe light frequency ω_p to the central frequency ω_{cav} of the ccw WGM. The characteristic time of the feedback loop can be as short as $10\,\mu$s [15]. The frequency stability (i.e., Allan deviation) of the probe laser is assessed by the beat note between the locked probe laser and a high-Q reference laser whose stability much exceeds both probe laser and microsphere [Fig. 1(a)]. Thus, the stability of the microcavity is indirectly measured.

The LSPR of gold nanorods (circular cross-section diameter of 10 nm and length of 35 nm) is utilized to enhance the ligand molecule-microcavity interaction (i.e., optoplasmonic sensing). These metal nanoparticles are permanently adsorbed to the microsphere's surface [9] and coupled to the evanescent field of the microcavity, thereby boosting the near-field intensity within the hotspot regions [Fig. 1(b)]. Each nanorod has two hotspots. The surface of each nanorod is modified with many receptor molecules, enabling a label-free detection of specific ligand molecules [Fig. 1(c)]. In the following, we assume that the receptor-ligand pair consists of partially mismatched single DNA strands [9]. Nevertheless, the

sensing scheme is applicable to other receptor-ligand pairs. We compute the longitudinal LSPR spectrum of the nanorod by using the finite-difference time-domain method. Figure 1(b) illustrates that the LSPR spectrum is peaked at 780 nm. The nanorod's electric polarizability at λ_{cav} is evaluated as $\alpha_{\text{NR}} = 0.96 \times 10^{-22} + i1.73 \times 10^{-22}$ m^3. The enhancement factor of the electric-field intensity around the nanorod's hotspots reaches $\Lambda = 800$ [9].

The typical number of the adsorbed nanorods in experiment is $N = 5$. In the ideal situation, the longitudinal direction of all nanorods is perpendicular to the equatorial plane of the microsphere. The complementary single DNA strands, i.e., ligands, are injected into the solution. Since the receptor and ligand strands are partially mismatched, the transient hybridization events [i.e., the spike events in the time trace of the WGM frequency as shown in Fig. 1(c)] occur primarily. We assume the sample solution is in the equilibrium state and neglect the permanent binding events [i.e., the step events as shown in Fig. 1(c)] in the following discussion. One ligand binding to one receptor located at a nanorod's hotspot gives rise to a polarizability increment, for instance, $\alpha_{\text{DNA}} \approx 2.5 \times 10^{-25}$ m^3 for the short oligonucleotides [9], to the corresponding nanorod. Normally, such a small polarizability increment cannot be detected by the WGM microcavity in the absence of the LSPR.

The experimental measurement has demonstrated that two degenerate cw and ccw WGMs are indirectly coupled via the backscattering and Rayleigh scattering of the nanoparticles [16–18], leading to the mode shift and broadening and the degeneracy lifting. This can be described by the following equation of motion for the amplitudes $\mathcal{A}_{\text{cw,ccw}}$ of two WGMs (Appendix)

$$\begin{pmatrix} \dot{\mathcal{A}}_{\text{cw}} \\ \dot{\mathcal{A}}_{\text{ccw}} \end{pmatrix} = \left[-\frac{\kappa}{2} + i(\omega_p - \omega_{\text{cav}}) \right] \begin{pmatrix} \mathcal{A}_{\text{cw}} \\ \mathcal{A}_{\text{ccw}} \end{pmatrix}$$
$$- \sum_{j=1}^{N} \left(\frac{\Gamma_j}{2} - i\Delta_j \right) \begin{pmatrix} 1 & e^{i\phi_j} \\ e^{-i\phi_j} & 1 \end{pmatrix} \begin{pmatrix} \mathcal{A}_{\text{cw}} \\ \mathcal{A}_{\text{ccw}} \end{pmatrix}$$
$$- \sqrt{\kappa_{\text{in}}} \begin{pmatrix} 0 \\ \mathcal{A}_p \end{pmatrix}, \tag{3}$$

with $\kappa = \kappa_0 + \kappa_{\text{in}}$. Here, ϕ_j is the phase difference between cw and ccw optical waves at the position of the jth nanorod. In the numerical simulation, ϕ_j is produced according to the uniform distribution of the gold nanorods in the equatorial circumference of the microsphere. The probe beam $\mathcal{A}_p$ is only coupled with the ccw WGM. The Rayleigh scattering rate and mode frequency shift caused by the jth nanorod are expressed as

$$\Gamma_j = \frac{(\alpha_{\text{NR}}^2 + \Lambda\alpha_j^2)\omega_{\text{cav}}^4}{6\pi(c/n)^3 V_{\text{cav}}}, \quad \Delta_j = \frac{(\alpha_{\text{NR}} + \Lambda\alpha_j)\omega_{\text{cav}}}{2V_{\text{cav}}}, \tag{4}$$

respectively. The extra time-dependent polarizability of the jth nanorod is given by

$$\alpha_j = \sum_k \left[\Theta(t - t_{j,k}^{\text{on}}) - \Theta(t - t_{j,k}^{\text{off}}) \right] \alpha_{\text{DNA}}, \tag{5}$$

where $\Theta(t)$ is the unit step function and $t_{j,k}^{\text{on}}$ ($t_{j,k}^{\text{off}}$) denotes the initial (end) time of the binding interaction between the kth ligand and a receptor on the jth nanorod.
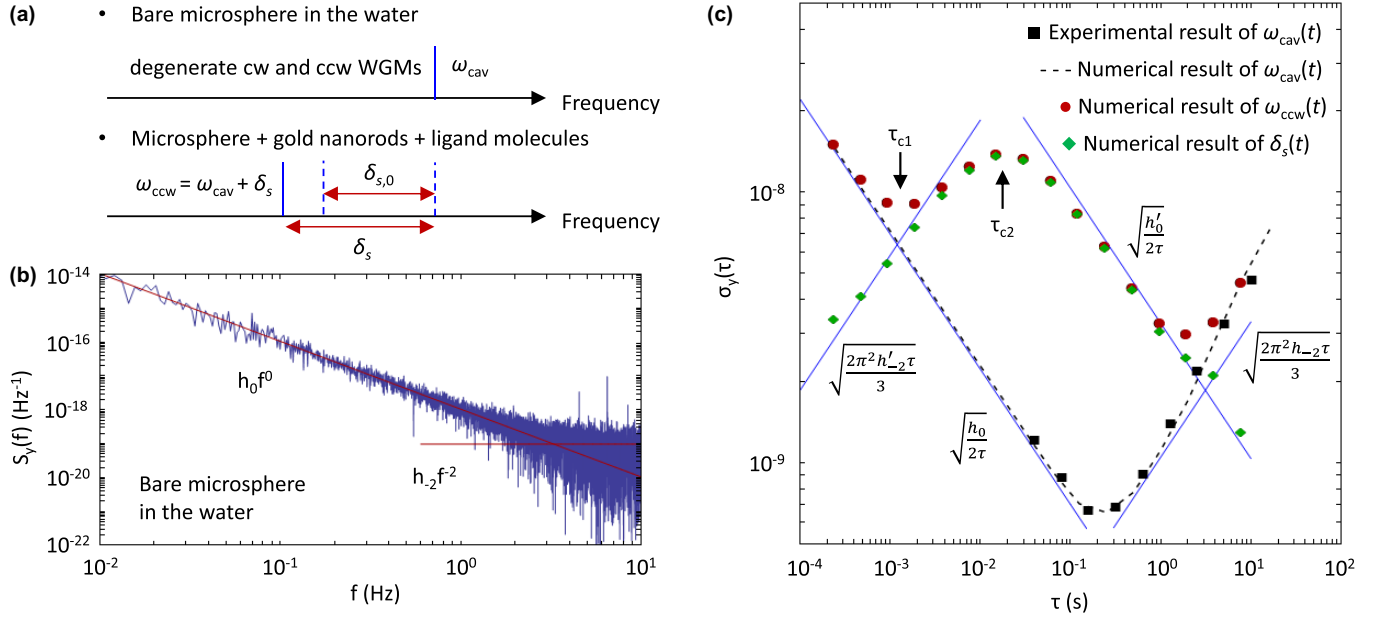
FIG. 2. (a) Frequency relations. The cw and ccw WGMs are degenerate for the bare microsphere in the water. The resonance frequency of two WGMs is ω_{cav}. When the gold nanorods are adsorbed to the surface of the microsphere, the resonance frequency ω_{ccw} of the ccw WGM is shifted from ω_{cav} by an amount of $\delta_{s,0}$. When the ligand molecules further bind to the gold nanorods, the total frequency shift of the ccw WGM is δ_s, i.e., $\omega_{ccw} = \omega_{cav} + \delta_s$. (b) Typical power spectral density $S_y(f)$ of the frequency noise in $\omega_{cav}(t)$ measured in experiment. The bare microsphere, i.e., without the gold nanorods and in the absence of the receptor-ligand binding interactions, is immersed in the water. (c) Allan deviation $\sigma_y(\tau)$. The square symbol denotes the stability of the experimentally-measured frequency ω_{cav} of the microsphere in the aqueous environment. The corresponding numerical simulation result is given by the dashed line. The circle symbol is the numerical result of the spike-event-perturbed frequency ω_{ccw} with $R = 250\,\mathrm{s}^{-1}$, $T = 244\,\mathrm{s}$, and $\tau_{ave} = 10^{-2}\,\mathrm{s}$. The diamond symbol corresponds to the numerical simulation result of the spike-event-induced frequency shift δ_s. The solid curves denote the asymptotes.

The coupling between cw and ccw WGMs lifts their degeneracy. We focus on the ccw WGM since the probe laser is locked to it. The transmission of the ccw wave

$$S_{\mathrm{Tran}}(\omega_p) = \frac{|\mathcal{A}_{ccw}(t)|^2}{\kappa_{in}|\mathcal{A}_p|^2},\qquad(6)$$

as a function of the probe light frequency ω_p can be derived from Eq. (3). The spectrum $S_{\mathrm{Tran}}(\omega_p)$ is single-peaked at $(\omega_{cav} + \delta_s)$ with a linewidth $(\kappa + \delta_b)$. That is to say, the mode splitting is unresolvable due to the relatively large cavity loss rate κ [19]. The extra spectral shift $\delta_s(t)$ and broadening $\delta_b(t)$ are caused by the nanorods and the receptor-ligand binding interactions. In what follows, we may set $\omega_p = \omega_{ccw}$ with the central frequency of the ccw WGM

$$\omega_{ccw}(t) = \omega_{cav}(t) + \delta_s(t),\qquad(7)$$

for the reasons: (1) The frequency locking time of the feedback loop is much shorter than the time scale of interest; and (2) The extra servo and photon shot noises are sufficiently low. Figure 2(a) summaries the relations among ω_{cav}, ω_{ccw}, and δ_s. We use $\delta_{s,0}$ to refer to the mode-shift component caused solely by the gold nanorods in the absence of the receptor-ligand interactions.

Next, we consider the numerical simulation of the receptor-ligand binding events. The experimental observations [11–14] have manifested: (1) The statistics of the transient single-molecule events follow the Poisson distribution, that is, the probability of $K \in \mathbb{Z}$ spike events occurring within a fixed

period T is given by

$$p(K) = \frac{(RT)^K e^{-RT}}{K!}.\qquad(8)$$

The total event rate is equal to $R = \sum_{j=1}^N r_j$ (in units of s^{-1}) with the event rate r_j of the jth nanorod. We neglect the difference between gold nanorods and have $R = Nr$ with $r = r_j$. The typical R in the conventional optoplasmonic sensing experiments is less than $1\,\mathrm{s}^{-1}$ for various ligand molecules [11,12]. Raising the ligand concentration enhances R. However, the higher R regime has thus far been difficult to analyze for the reason of the limited time resolution. Distinguishing the single-molecule events requires the time resolution to be much shorter than R^{-1}. The time resolution of the conventional optoplasmonic sensors is limited by $\sim 20\,\mathrm{ms}$ because of the slow scanning rate of the probe beam [11–14]; and (2) The duration $(t_{j,k}^{off} - t_{j,k}^{on})$ of the single-molecule binding interaction follows the exponential distribution with an average duration τ_{ave}. When $\tau_{ave} < R^{-1}$, different single-molecule events are distinguishable. By contrast, different single-molecule events are overlapped when $\tau_{ave} > R^{-1}$. Again, the current experimental detection is limited by $\tau_{ave} \sim 20\,\mathrm{ms}$. As we will see below, our sensing scheme may overcome this restriction.

Indeed, R and τ_{ave} are directly linked to the kinetic on-rate $k_{on} = R/c$ [11] and off-rate $k_{off} = 1/\tau_{ave}$ [13] constants. Here, c denotes the ligand concentration. In some literature, both k_{on} and k_{off} are normalized per nanorod. Measuring R and τ_{ave} allows one to derive the kinetic properties of the receptor-ligand

binding interactions. For examples, conventional optoplasmonic sensing experiments have measured $k_{on} = 0.53 \times 10^3$ and 3.8×10^3 $M^{-1}s^{-1}$ for the gold nanorods interacting with Hg^{2+} and Zn^{2+} ions [11], respectively, and $k_{off} = 47$ and 23 s^{-1} for the primer/template DNA interacting with Thermus aquaticus and Klenow fragment DNA polymerases [13], respectively.

The above two experimental manifestations allow one to numerically predict $t_{j,k}^{on}$ and $t_{j,k}^{off}$ in a time trace (length of T) of $\omega_{ccw}(t)$. The specific numerical simulation processes are summarized as follows: (1) Generate a series of random times (number of K) according to the Poisson distribution with the event rate R and the time length T. Each time point corresponds to the initial time of a spike event; (2) Create K uniformly distributed random integers within $[1, N]$ and map this array onto the time series generated in the step (1). Thus, one obtains the initial times of different single-molecule binding events in Eq. (5), $t_{j,k}^{on}$ with $j \in [1, N]$ and $k \in [1, K]$; and (3) Generate a series of random time intervals τ_k according to the exponential distribution with the average duration τ_{ave}. As a result, the end times of different binding events in Eq. (5) are given by $t_{j,k}^{off} = t_{j,k}^{on} + \tau_k$. Once obtaining $t_{j,k}^{on}$ and $t_{j,k}^{off}$, one may simulate the time-dependent central frequency $\omega_{ccw}(t)$ of the ccw WGM through Eqs. (3)–(5).

III. RESULTS AND ANALYSIS

Let us focus on the stability of the frequency fluctuation signal

$$y(t) = \omega_{ccw}(t)/\omega_0 - 1, \tag{9}$$

whose power spectral density is given by

$$S_y(f) = |\mathcal{F}[y(t)]|^2 = \left| \int y(t)e^{-i2\pi ft}dt \right|^2. \tag{10}$$

Here, $\omega_0 = 2\pi \times 382$ THz is the constant central frequency of the ccw WGM. We first consider $y(t)$ in the absence of $\delta_s(t)$ and the reduced signal $y(t) = \omega_{cav}(t)/\omega_0 - 1$ with $\delta_s = 0$ represents a bare microsphere in the aqueous environment. Figure 2(b) shows a typical $S_y(f)$ of the bare microsphere measured in experiment. It is seen that $y(t)$ is mainly composed of the white frequency ($\propto f^0$) and random walk ($\propto f^{-2}$) noises. The stability of $y(t)$ is evaluated by the Allan deviation $\sigma_y(\tau)$ with a sampling time τ [20,21]. The white frequency noise originates from the microsphere's thermal Brownian motion [22,23] that leads to a $\frac{1}{\sqrt{\tau}}$-dependence of the short-term ($\tau < 0.1$ s) stability [24],

$$\sigma_y(\tau) = \sqrt{\frac{h_0}{2\tau}}. \tag{11}$$

By contrast, the random walk noise arises from the linear frequency drift and raises $\sigma_y(\tau > 0.1 \text{ s})$ with a scaling factor $\sqrt{\tau}$ [24],

$$\sigma_y(\tau) = \sqrt{\frac{2\pi^2 h_{-2}\tau}{3}}. \tag{12}$$

Additionally, $\sigma_y(\tau)$ displayed in Fig. 2(c) manifests the existence of the flicker walk ($\propto f^{-3}$) component, which gives $\sigma_y(\tau) \propto \tau$ for a large τ, in $y(t)$. As a result, $S_y(f)$ with

$\delta_s(t) = 0$ (i.e., the bare microsphere in the aqueous environment) takes the form

$$S_y(f) = h_0 f^0 + h_{-2} f^{-2} + h_{-3} f^{-3}, \tag{13}$$

with the typical values $h_0 = 0.98 \times 10^{-19}$ Hz^{-1}, $h_{-2} = 1.67 \times 10^{-19}$ Hz, and $h_{-3} = 2.22 \times 10^{-19}$ Hz^2 derived from the curve fitting. We have also estimated the fundamental thermorefractive-noise-limited stability [25,26],

$$\sigma_y^{TR}(\tau) = \frac{4 \times 10^{-13}}{\sqrt{\tau}}, \tag{14}$$

which is much lower than $\sqrt{h_0/2\tau}$. According to $S_y(f)$ with $\delta_s(t) = 0$, one may numerically generate the noise-perturbed $\omega_{cav}(t)$ via the method of digitally filtering the white noise [27]. As shown in Fig. 2(c), the Allan deviation of the numerically generated $\omega_{cav}(t)$ well matches the experimental measurement.

After obtaining $t_{j,k}^{on}$, $t_{j,k}^{off}$, and $\omega_{cav}(t)$, we numerically simulate the time trace of the mode frequency $\omega_{ccw}(t)$ by means of calculating the transmission spectrum $S_{Tran}(\omega_p = \omega_{ccw})$ from Eqs. (3)–(6). In the presence of the transient spike events [i.e., $\delta_s(t) \neq 0$], the Allan deviation of $y(t)$ exhibits a distinct behavior compared to that of $\delta_s(t) = 0$. As shown in Fig. 2(c), $\sigma_y(\tau)$ for $\omega_{ccw}(t)$ with $\delta_s(t) \neq 0$ goes up firstly at the sampling time $\tau = \tau_{c1}$ and then degrades at $\tau = \tau_{c2}$. Understanding the underlying mechanism relies on extracting the spike-event noise $\delta_s(t)$ from $\omega_{ccw}(t)$. This is feasible in the numerical simulation but challenging in experiment.

As depicted in Fig. 3(a), multiple spikes are presented in the time trace of $\delta_s(t)$, where we have removed the constant bias $\delta_{s,0}$ caused by the gold nanorods. The Fourier analysis

$$S_{(\delta_s/\omega_0)}(f) = |\mathcal{F}[\delta_s(t)/\omega_0]|^2, \tag{15}$$

illustrates that $\delta_s(t)$ predominantly consists of the white frequency $h_0' f^0$ and random walk $h_{-2}' f^{-2}$ noises [Fig. 3(b)],

$$S_{(\delta_s/\omega_0)}(f) = h_0' f^0 + h_{-2}' f^{-2}. \tag{16}$$

The cross between $h_0' f^0$ and $h_{-2}' f^{-2}$ occurs at

$$f_{c2} = \frac{\sqrt{3}}{2\pi\tau_{c2}}. \tag{17}$$

The random walk component strongly raises the Allan deviation of $\delta_s(t)/\omega_0$, i.e., following the $\sqrt{2\pi^2 h_{-2}'\tau/3}$ line, until hitting the $\sqrt{h_0'/2\tau}$ line that is determined by the white frequency noise [Fig. 2(c)]. This coincides with the corresponding behavior of the Allan deviation $\sigma_y(\tau)$ of $\omega_{ccw}(t)$ with $\delta_s(t) \neq 0$.

Using Eq. (3), one predicts that a ligand interacting with a receptor gives rise to a 10-fm increment of δ_s. That is, the single-molecule-induced mode shift is 10 fm. The spike heights in Fig. 3(a) are closely related to the single-molecule event rate R and the average event duration τ_{ave}. The reciprocal of R measures the average interval between the initial times of two adjacent receptor-ligand binding events. When R^{-1} exceeds the average duration τ_{ave}, a ligand may start to interact with a receptor before the end of another receptor-ligand binding event. This results in an overlap of different binding events, i.e., multimolecular events, and a
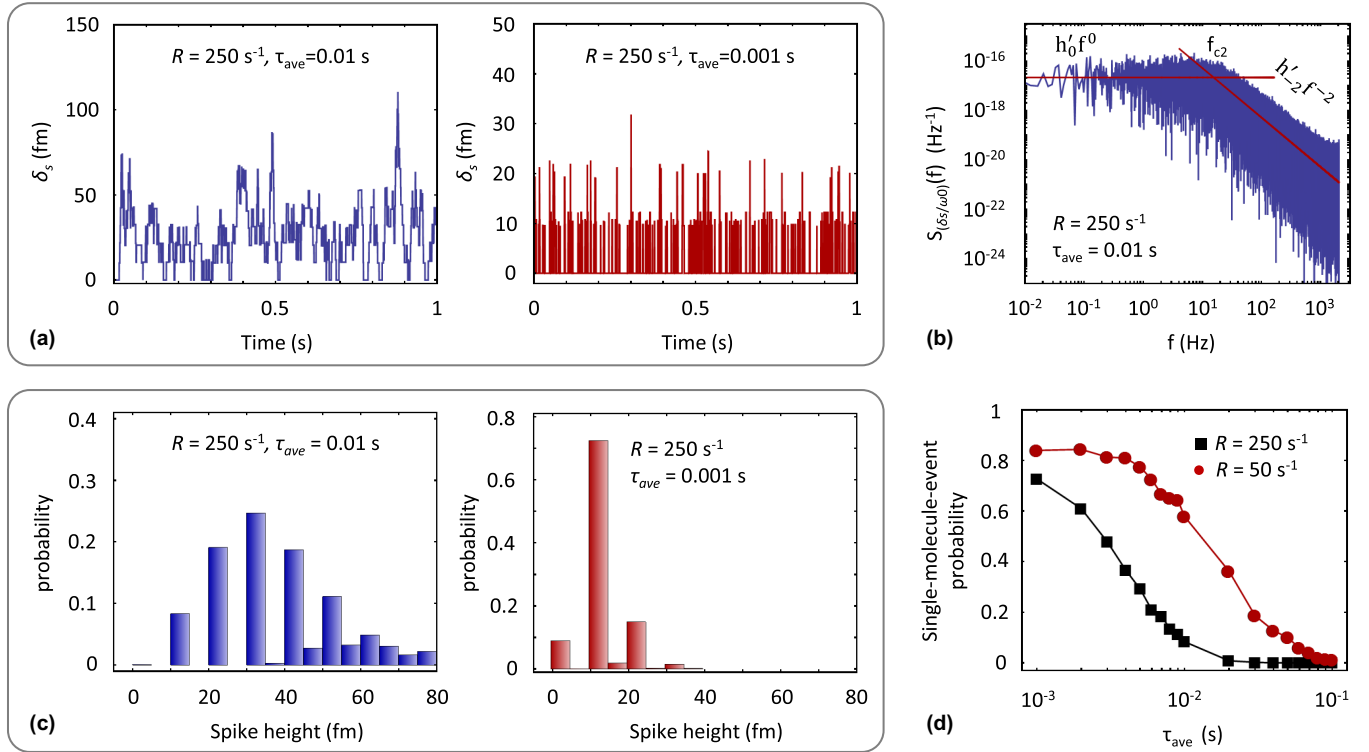
FIG. 3. (a) Numerically simulated traces of the spike-event-induced mode shift $\delta_s(t)$ in units of fm. The constant bias $\delta_{s,0}$ caused by the gold nanorods has been removed. A ligand binding to a receptor causes an about 10-fm shift. (b) Power spectral density $S_{(\delta_s/\omega_0)}(f)$ of the numerically simulated $\delta_s(t)$. The curve fitting illustrates $S_{(\delta_s/\omega_0)}(f) = h'_0 f^0 + h'_{-2} f^{-2}$ with $h'_0 = 2.14 \times 10^{-17}$ Hz^{-1} and $h'_{-2} = 5.20 \times 10^{-15}$ Hz. (c) Distribution of spike heights extracted from the numerical simulation. The bins around 10 fm correspond to the single-molecule events. (d) Probability of the single-molecule events extracted from the numerical simulation vs the average duration τ_{ave} for different event rates R.

spike higher than 10 fm. Figure 3(c) displays the statistical distribution of the spike heights extracted from Fig. 3(a). It is seen that when $R\tau_{\text{ave}} > 1$ the distribution is maximized at a spike height of about $R\tau_{\text{ave}} \times 10$ fm. By contrast, the distribution is maximized at 10 fm for $R\tau_{\text{ave}} < 1$, indicating that the single-molecule events take the predominant role.

Figure 3(d) illustrates the dependence of the single-molecule-event probability on the average duration τ_{ave}. A short τ_{ave} highlights the probability of the single-molecule events. Shortening τ_{ave} relies on weakening the receptor-ligand interaction, for instance, increasing the number of mismatched bases between receptor and ligand single DNA strands [9]. However, a short τ_{ave} also demands a fast feedback loop. The frequency locking time of 10 μs is feasible in experiment [15]. Thus, τ_{ave} can be, in principle, as short as 10 μs, which is over 10^3 times smaller than the current resolution time limit $\sim$20 ms of the conventional optoplasmonic sensors [11–14].

We use Δ_{ave} to denote the average height of different spikes in a time trace of $\delta_s(t)$. It is impractical to directly derive the analytical expression of Δ_{ave}. Here, we introduce the empirical equation

$$\Delta_{\text{ave}} = [(R\tau_{\text{ave}}) + (1 + R\tau_{\text{ave}})^{-1/2m}] \times 10 \text{ fm}, \quad (18)$$

where the curve fitting gives $m = 2$. The validity of this expression is confirmed by Fig. 4(a). In the limit of $R\tau_{\text{ave}} \ll 1$, Eq. (18) is reduced to $\Delta_{\text{ave}} \approx 10$ fm, i.e., the

single-molecule spike events predominate. By contrast, $R\tau_{\text{ave}} \gg 1$ leads to $\Delta_{\text{ave}} \approx (R\tau_{\text{ave}}) \times 10$ fm, i.e., $(R\tau_{\text{ave}})$ individual receptor-ligand binding events overlap each other.

Figures 4(b) and 4(c) plot the dependence of the white frequency parameter h'_0 on τ_{ave} and R, respectively, which is derived from the numerical simulation. It is seen that $\log_{10} h'_0$ goes up almost linearly as $\log_{10} \tau_{\text{ave}}$ and $\log_{10} R$ are increased. We suggest the following empirical formula

$$h'_0 = I\delta t, \quad (19)$$

with the intensity of the spike-induced fluctuations

$$I = (\Delta_{\text{ave}}/\omega_0)^2, \quad (20)$$

and the fluctuation time scale

$$\delta t = \left[\frac{2}{1 + (R\tau_{\text{ave}})^{-2}} \right]^m \sqrt{\frac{\tau_{\text{ave}}}{R}}, \quad (21)$$

where the curve fitting gives $m = 2/3$. By contrast, varying τ_{ave} hardly changes the random walk parameter $\log_{10} h'_{-2}$ while $\log_{10} h'_{-2}$ vs $\log_{10} R$ exhibits a linear behavior. One may write the following empirical formula

$$h'_{-2} = AI_0 R, \quad (22)$$

where $I_0 = (10 \text{ fm}/\omega_0)^2$ and the curve fitting gives $A \approx 10$. We have also evaluated the cross times τ_{c1} and τ_{c2} from the numerical simulation [Fig. 4(b)]. It is found that τ_{c1} rarely depends on τ_{ave}, corresponding to the behavior of h'_{-2}. By
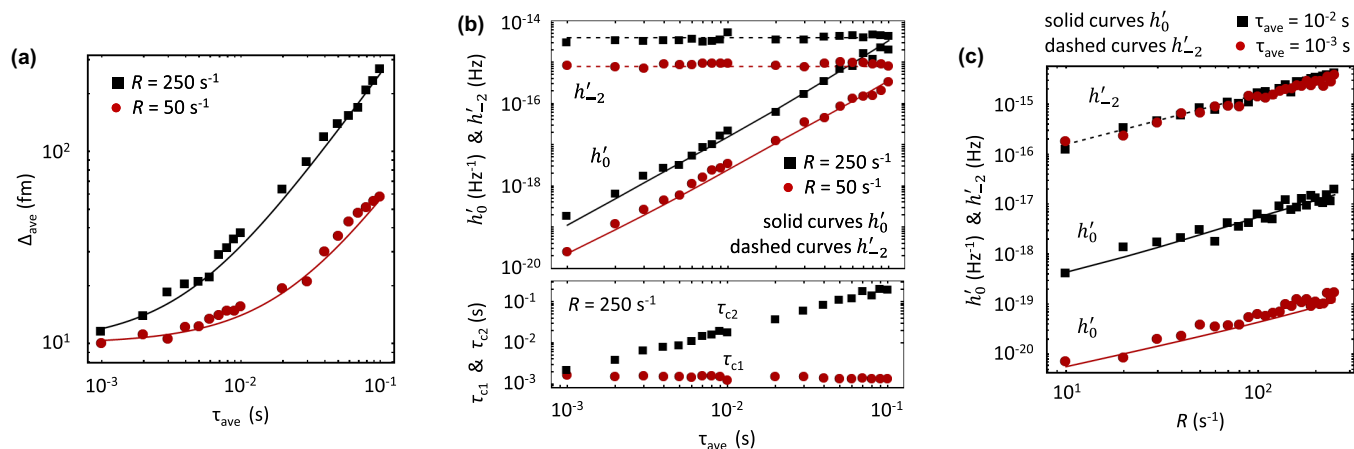
FIG. 4. (a) Dependence of the average spike height Δ_{ave} in a time trace of $\delta_s(t)$ on the average duration τ_{ave} with different event rates R. The solid lines correspond to the results of the empirical formula (18). (b) Upper panel: White frequency h'_0 and random walk h'_{-2} parameters vs R. The solid lines correspond to the results of the empirical formula (19) while the dashed lines denote the results of the empirical equation (22). Lower panel: Cross times τ_{c1} and τ_{c2} as a function of τ_{ave} with $R = 250$ s^{-1}. (c) White frequency h'_0 and random walk h'_{-2} parameters vs τ_{ave}. In all plots, the filled square and circle symbols denote the numerical simulation results.

contrast, τ_{c1} scales as $\sqrt{h'_0}$ since τ_{c1} is determined by the cross between $\sqrt{h'_0/2\tau}$ and $\sqrt{2\pi^2 h'_{-2}\tau/3}$.

Finally, we come to the question of how to derive the single-molecule event rate R and the average duration τ_{ave} from the stability measurement of the mode frequency $\omega_{ccw}(t)$. In experiment, it is challenging to extract the mode shift $\delta_s(t)$ from the time trace of $\omega_{ccw}(t)$. Nevertheless, the values of h_0, h'_0, τ_{c1} and τ_{c2} can be obtained directly from the Allan deviation of $\omega_{ccw}(t)$ in the absence and presence of the receptor-ligand binding interactions. The random walk noise in $\delta_s(t)$ is then evaluated by $h'_{-2} = h'_0 f_{c2}^2$, where the cross frequency f_{c2} is given by Eq. (17). Using the empirical formulas (18)–(22), one obtains R and τ_{ave} and further derive the kinetic rate constants k_{on} and k_{off}. It should be noted that the intrinsic fluctuations in $\omega_{cav}(t)$ need to be suppressed sufficiently so that h_0 and h_{-2} are lower than h'_0 and h'_{-2}, respectively. Otherwise, the spike events are deeply submerged in the background noise. This requires a high Q factor of the microsphere in the aqueous environment and a large polarizability of the ligand molecules.

IV. DISCUSSION

In summary, we have numerically studied a frequency-locking-based single-molecule sensing scheme. The kinetic properties of a specific chemical/biological reaction may be assessed by simply measuring the Allan deviation of the frequency-locked probe beam. This approach is potentially applicable to an aqueous solution with a high ligand concentration and rapid receptor-ligand interactions. The current microcavity technology is ready to implement this sensing scheme.

Conventional optoplasmonic sensing is mainly based on the resonance frequency shift that is derived from the transmission spectrum of the WGM microcavity. To capture the complete WGM spectrum, the probe laser is slowly scanned over a wide spectral range around the WGM resonance frequency, resulting in a typical time resolution of ~20 ms. Such

a relatively long time resolution of the detection restricts the relevant sensing applications. For instance, the conventional optoplasmonic sensors cannot respond to the rapid binding interactions between partially mismatched single DNA strands [9]. Also, the ligand concentration in an aqueous solution should be appropriately low (e.g., fM ∼ nM in [11–14]) so that the sensors can distinguish different single-molecule events. In comparison, the time resolution of the frequency-locking-based sensing scheme studied in this work is mainly determined by the feedback loop. The frequency locking time can be as short as 10 μs [15], potentially enabling the sensors to monitor the rapid hybridization reactions of single stranded DNA molecules and identifying the single-molecule events with a high ligand concentration.

Besides the resonance-frequency-shift-based sensing mechanism, single molecules may also be detected through the mode splitting that results from the scatterer-induced coupling between cw and ccw WGMs [17]. The mode-splitting mechanism enables the self-referenced detection, where the beat note between two split modes is measured, leading to a superior noise suppression [28]. Equation (3) is also applicable to study the mode-splitting mechanism. However, observing the mode splitting requires a high enough Q (usually, $Q > 10^8$) factor of the microsphere, which is challenging in the aqueous environment [5]. In addition, the polarizability α of the ligand molecules should be large enough to give rise to a strong indirect coupling between cw and ccw WGMs. This is quantified by the condition $\alpha > V_{cav}/Q$ [8]. For our specific sensor, the mode splitting resolvability demands $\alpha > 7.2 \times 10^{-21}$ m^3. Consequently, the mode-splitting mechanism significantly restricts its applications for detecting small-polarizability single molecules.

In our sensing scheme, the detection time is shortened by locking the probe beam to the microcavity, instead of directly monitoring the transmission spectrum of the microcavity as in conventional sensing schemes. Further shortening the detection time requires a faster capture of the complete WGM spectrum. This may be implemented by measuring the

ring-up signal from the WGM microcavity that is driven by a sequence of far-detuned light pulses [29]. Cavity ring-up spectroscopy allows one to acquire single-molecule-induced effects at nanosecond timescales. Combining the Allan deviation analysis with the cavity ring-up technique potentially paves the path for the study of ultrafast biochemical reactions.

APPENDIX: BACKSCATTERING AND RAYLEIGH SCATTERING

In this section, we derive the equations of motion for the cw and ccw WGMs that are indirectly coupled through the backscattering and Rayleigh scattering of a tiny dipole scatterer (e.g., atom, molecule, and nanoparticle) located in the vicinity of the microcavity [17]. The scatterer is modeled by a two-state (upper $|e\rangle$ and lower $|g\rangle$ with an energy separation ω_A) system with the relevant operators $\sigma_{eg} = |e\rangle\langle g|$, $\sigma_{ge} = |g\rangle\langle e|$ and $\sigma_z = |e\rangle\langle e| - |g\rangle\langle g|$. The annihilation and creation operators for the cw (ccw) WGM are $a_{\rm cw}$ ($a_{\rm ccw}$) and $a_{\rm cw}^\dagger$ ($a_{\rm ccw}^\dagger$), respectively. The coupling strengths between the scatterer and two WGMs are

$$g_{\rm cw,ccw} = -\mathbf{d} \cdot \mathbf{u}_{\rm cw,ccw}(\mathbf{r}_0)/\hbar, \tag{A1}$$

where $\mathbf{u}_{\rm cw,ccw}(\mathbf{r})$ are the normalized mode vectors of two WGMs, $\mathbf{d}$ is the scatterer's dipole moment vector and $\mathbf{r}_0$ denotes the scatterer's location. The approximate solutions of $\mathbf{u}_{\rm cw,ccw}(\mathbf{r})$ may be obtained from Ref. [30]. The scatterer also interacts with the (vacuum) bosonic reservoir, where the jth boson mode is characterized by the oscillation frequency ω_j, the annihilation b_j and creation $b_j^\dagger$ operators and the boson mode-scatterer coupling strength

$$g_j = \sqrt{\frac{\omega_j}{2\hbar\varepsilon_0 V_{\rm vac}}}|\mathbf{d}|, \tag{A2}$$

with the quantization volume $V_{\rm vac}$.

The Hamiltonian H for the interacting system is written as

$$H/\hbar = \omega_{\rm cav}a_{\rm cw}^\dagger a_{\rm cw} + \omega_{\rm cav}a_{\rm ccw}^\dagger a_{\rm ccw}$$
$$+ \frac{\omega_A}{2}\sigma_z + \sum_j \omega_j b_j^\dagger b_j$$

$$- [\sigma_{eg}(g_{\rm cw}a_{\rm cw} + g_{\rm ccw}a_{\rm ccw}) + \text{H.c.}]$$
$$+ \left[\sigma_{eg}\sum_j g_j b_j + \text{H.c.}\right]. \tag{A3}$$

In the Heisenberg picture, one may derive the following equations

$$\dot{a}_{\rm cw} = (-\kappa_0/2 - i\omega_{\rm cav})a_{\rm cw} + ig_{\rm cw}^*\sigma_{ge}, \tag{A4a}$$

$$\dot{a}_{\rm ccw} = (-\kappa_0/2 - i\omega_{\rm cav})a_{\rm ccw} + ig_{\rm ccw}^*\sigma_{ge}, \tag{A4b}$$

$$\dot{\sigma}_{ge} = (-\gamma/2 - i\omega_A)\sigma_{ge} - ig_{\rm cw}a_{\rm cw}\sigma_z$$
$$- ig_{\rm ccw}a_{\rm ccw}\sigma_z - i\sigma_z\sum_j g_j b_j, \tag{A4c}$$

$$\dot{b}_j = -i\omega_j b_j + ig_j^*\sigma_{ge}, \tag{A4d}$$

where we have also inserted the cavity-loss and polarization-decay (rate γ) terms. The above equations indicate that the cw and ccw waves are indirectly coupled through the photon scattering of the scatterer. In the weak-coupling limit, the scatterer is mainly in the lower state $|g\rangle$ and one has the approximation $\sigma_z \approx -1$. Further, we use the Weisskopf-Wigner approach to eliminate σ_{ge} and b_j [16] and arrive at

$$\begin{pmatrix} \dot{a}_{\rm cw} \\ \dot{a}_{\rm ccw} \end{pmatrix} = \left[-\frac{\kappa}{2} - i\omega_{\rm cav} - \left(\frac{\Gamma}{2} - i\Delta\right) \right.$$
$$\left. \times \begin{pmatrix} 1 & e^{i\phi} \\ e^{-i\phi} & 1 \end{pmatrix} \right] \begin{pmatrix} a_{\rm cw} \\ a_{\rm ccw} \end{pmatrix}. \tag{A5}$$

Here, ϕ is the phase difference between cw and ccw waves at $\mathbf{r}_0$ and the scatterer's polarizability is defined as

$$\alpha = \frac{|\mathbf{d}|^2}{\hbar\varepsilon_0} \frac{1}{\omega_A - \omega_{\rm cav} - i\gamma/2}. \tag{A6}$$

The Rayleigh scattering rate Γ and frequency shift Δ caused by the scatterer are respectively given by

$$\Gamma = \frac{\alpha^2\omega_{\rm cav}^4}{6\pi(c/n)^3 V_{\rm cav}}, \quad \Delta = \frac{\alpha\omega_{\rm cav}}{2V_{\rm cav}}, \tag{A7}$$

with the refractive index n of the environment medium. Thus, the backscattering and Rayleigh scattering of the scatterer lead to the spectral shift and broadening of WGMs. We further replace the photon operators $a_{\rm cw,ccw}$ with their c-number counterparts $\mathcal{A}_{\rm cw,ccw}$ due to the classical laser lights in experiment. After extending the above analysis to a system containing multiple scatterers and including the prism-microcavity coupling, one obtains Eq. (3) in the main text.

[1] F. Vollmer and D. Yu, *Optical Whispering Gallery Modes for Biosensing: From Physical Principles to Applications* (Springer International Publishing, Cham, 2020).

[2] F. Vollmer, D. Braun, A. Libchaber, M. Khoshsima, I. Teraoka, and S. Arnold, Protein detection by optical shift of a resonant microcavity, Appl. Phys. Lett. **80**, 4057 (2002).

[3] S. Arnold, M. Khoshsima, I. Teraoka, S. Holler, and F. Vollmer, Shift of whispering-gallery modes in microspheres by protein adsorption, Opt. Lett. **28**, 272 (2003).

[4] F. Vollmer, S. Arnold, and D. Keng, Single virus detection from the reactive shift of a whispering-gallery mode, Proc. Natl. Acad. Sci. USA **105**, 20701 (2008).

[5] M. L. Gorodetsky, A. A. Savchenkov, and V. S. Ilchenko, Ultimate Q of optical microsphere resonators, Opt. Lett. **21**, 453 (1996).

[6] D. K. Armani, T. J. Kippenberg, S. M. Spillane, and K. J. Vahala, Ultra-high-Q toroid microcavity on a chip, Nature **421**, 925 (2003).

[7] M. Pöllinger, D. O'Shea, F. Warken, and A. Rauschenbeutel, Ultrahigh-Q Tunable Whispering-Gallery-Mode Microresonator, Phys. Rev. Lett. **103**, 053901 (2009).

[8] W. Kim, Ş. K. Özdemir, J. Zhu, and L. Yang, Observation and characterization of modesplitting in microsphere resonators inaquatic environment, Appl. Phys. Lett. **98**, 141106 (2011).

[9] M. D. Baaske, M. R. Foreman, and F. Vollmer, Single-molecule nucleic acid interactions monitored on a label-free microcavity biosensor platform, Nat. Nanotech. **9**, 933 (2014).

[10] J. D. Swaim, J. Knittel, and W. P. Bowen, Detection limits in whispering gallerybiosensors with plasmonic enhancement, Appl. Phys. Lett. **99**, 243109 (2011).

[11] M. D. Baaske and F. Vollmer, Optical observation of single atomic ions interacting with plasmonic nanorods in aqueous solution, Nat. Photon. **10**, 733 (2016).

[12] E. Kim, M. D. Baaske, and F. Vollmer, In situ observation of single-molecule surface reactions from low to high affinities, Adv. Mater. **28**, 9941 (2016).

[13] E. Kim, M. D. Baaske, I. Schuldes, P. S. Wilsch, and F. Vollmer, Label-free optical detection of single enzyme-reactant reactions and associated conformational changes, Sci. Adv. **3**, e1603044 (2017).

[14] S. Vincent, S. Subramanian, and F. Vollmer, Optoplasmonic characterisation of reversible disulfide interactions at single thiol sites in the attomolar regime, Nat. Commun. **11**, 2043 (2020).

[15] G. Bianchini, P. Cancio, F. Minardi, F. S. Pavone, F. Perrone, M. Prevedelli, and M. Inguscio, Wide-bandwidth frequency locking of a 1083-nm extended-cavity DBR diode laser to a high-finesse Fabry-Pérot resonator, Appl. Phys. B **66**, 407 (1998).

[16] A. Mazzei, S. Götzinger, L. de S. Menezes, G. Zumofen, O. Benson, and V. Sandoghdar, Controlled Coupling of Counter-propagating Whispering-Gallery Modes by a Single Rayleigh Scatterer: A Classical Problem in a Quantum Optical Light, Phys. Rev. Lett. **99**, 173603 (2007).

[17] J. Zhu, S. K. Ozdemir, Y.-F. Xiao, L. Li, L. He, D.-R. Chen, and L. Yang, On-chip single nanoparticle detection and sizing by mode splitting in an ultrahigh-Q microresonator, Nat. Photon. **4**, 46 (2010).

[18] W. Chen, Ş. K. Özdemir, G. Zhao, J. Wiersig, and L. Yang, Exceptional points enhance sensing in an optical microcavity, Nature **548**, 192 (2017).

[19] S. Subramanian, S. Vincent, and F. Vollmer, Effective linewidth shifts in single-molecule detection using optical whispering gallery modes, Appl. Phys. Lett. **117**, 151106 (2020).

[20] D. W. Allan, Statistics of atomic frequency standards, Proc. IEEE **54**, 221 (1996).

[21] F. Riehle, *Frequency Standards: Basics and Applications* (Wiley-VCH, Weinheim, 2004).

[22] A. Schliesser, G. Anetsberger, R. Rivière, O. Arcizetand, and T. J. Kippenberg, High-sensitivity monitoring of micromechanical vibration using optical whispering gallery moderesonators, New J. Phys. **10**, 095015 (2008).

[23] M. Aspelmeyer, T. J. Kippenberg, and F. Marquardt, Cavity optomechanics, Rev. Mod. Phys. **86**, 1391 (2014).

[24] W. J. Riley, *Handbook of Frequency Stability Analysis*, NIST Special Publication 1065 (NIST, Boulder, 2008).

[25] M. L. Gorodetsky and I. S. Grudinin, Fundamental thermal fluctuations in microspheres, J. Opt. Soc. Am. B **21**, 697 (2004).

[26] G. Huang, E. Lucas, J. Liu, A. S. Raja, G. Lihachev, M. L. Gorodetsky, N. J. Engelsen, and T. J. Kippenberg, Thermorefractive noise in silicon-nitride microresonators, Phys. Rev. A **99**, 061801(R) (2019).

[27] D. Yu and R. Dumke, Open Ising model perturbed by classical colored noise, Phys. Rev. A **100**, 022124 (2019).

[28] B.-B. Li, W. R. Clements, X.-C. Yu, K. Shi, Q. Gong, and Y.-F. Xiao, Single nanoparticle detection using split-mode microcavity Raman lasers, Proc. Natl. Acad. Sci. USA **111**, 14657 (2014).

[29] S. Rosenblum, Y. Lovsky, L. Arazi, F. Vollmer, and B. Dayan, Cavity ring-up spectroscopy for ultrafast sensing with optical microresonators, Nat. Commun. **6**, 6788 (2015).

[30] B. E. Little, J.-P. Laine, and H. A. Haus, Analytic theory of coupling from tapered fibers and half-blocks into microsphere resonators, J. Lightwave Technol. **17**, 704 (1999).